

Emergent of the flat band and superstructures in the VSe₂ / Bi₂Se₃ system

Turgut Yilmaz^{1*}, Xiao Tong², Zhongwei Dai², Jerzy T. Sadowski², Eike F. Schwier³, Kenya Shimada³, Sooyeon Hwang², Kim Kisslinger², Konstantine Kaznatcheev¹, Elio Vescovo¹, and Boris Sinkovic⁴

¹National Synchrotron Light Source II, Brookhaven National Lab, Upton, New York 11973, USA

²Center for Functional Nanomaterials, Brookhaven National Lab, Upton, New York 11973, USA

³Hiroshima Synchrotron Radiation Center, Hiroshima University, 2-313 Kagamiyama, Higashi Hiroshima 739-0046, Japan

⁴Department of Physics, University of Connecticut, Storrs, Connecticut 06269, USA

*tyilmaz@bnl.gov

Dispersionless flat bands are proposed to be a fundamental ingredient to achieve the various sought after quantum states of matter including high-temperature superconductivity¹⁻⁴ and fractional quantum Hall effect⁵⁻⁶. Materials with such peculiar electronic states, however, are very rare and often exhibit very complex band structures. Here, we report on the emergence of a flat band with a possible insulating ground state in the sub-monolayer VSe₂ / Bi₂Se₃ heterostructure by means of angle-resolved photoemission spectroscopy and scanning tunneling microscopy. The flat band is dispersionless along the $k_{||}$ and k_z momenta, filling the entire Brillouin zone, and it exhibits a complex circular dichroism signal reversing the sign at several points of the Brillouin zone. These properties together with the presence of a Moiré patterns in VSe₂ suggest that the flat band is not a trivial disorder or confinement effect and could even be topologically non-trivial. Another intriguing finding is that the flat band does not modify the Dirac cone of Bi₂Se₃ around the Dirac point. Furthermore, we found that the flat band and the Dirac surface states of Bi₂Se₃ have opposite energy shifts

with electron doping. This opens a novel way of controlling the spin texture of photocurrents as well as the transport properties of the heterostructure. These features make this flat band remarkably distinguishable from previous findings and our methodology can be applied to other systems opening a promising pathway to realize strongly correlated quantum effects in topological materials.

The physics of solids is determined by their energy band structures. Therefore, investigation and controlling distinct electronic band dispersions are of great importance in condensed matter to understand and discover new states of the matter. One of the exotic electronic states is a type of flat band which is predicted to host high-temperature superconductivity¹⁻⁴, fractional quantum Hall effect (FQHE)⁵⁻⁶, and ferromagnetism⁷⁻⁹. In a superconductor, a flat band can boost the coupling constant and the transition temperature (T_c) because of the enhanced density of states at the Fermi level (E_F)¹⁰⁻¹¹. This was utilized to explain the unexpected superconductivity in rhombohedral graphite and twisted graphene¹²⁻¹⁴. Other examples of the flat band materials are Kagome lattices in which the flat band stems from the destructive quantum interference due to the frustrated lattice geometry⁷⁻⁸. The Kagome-type flat band was reported in FeSn and Fe₃Sn₂ by angle-resolved photoemission spectroscopy (ARPES) and in Co₃Sn₂S₂ by scanning tunneling spectroscopy (STS)⁸⁻¹⁰. However, the complexity of the electronic structure in photoemission data and the lack of momentum resolution in STS make the observations elusive. Another system with the dispersionless flat electronic states could be the Mott insulators in which the strong correlation effect forms the flat Hubbard band with an insulating gap the E_F as predicted in TaS_{2-x}Se_x and NbS_{2-x}Se_x¹⁵⁻¹⁸. The strong correlation effect was also investigated in Bi₂Se₃ and Bi₂Te₂Se topological insulators (TI) and a possible p-band Mott insulating state where the Hubbard bands were predicted to exist in these samples¹⁹⁻²¹. The experimental signature of the Mott insulating

state was also captured in multilayer graphene Moiré superlattice indicating the strong correlation effect in that system²². Computational efforts were also focused on designing the flat band transition metal dichalcogenides (TMDs) Moiré superlattices which could support strongly correlated physics at higher-temperatures due to the flat bands²³⁻²⁵. Thereby, the previous works conclude that the flat band media could be fertile to many novel states of the matter. However, apart from Mott insulators, the limited number of the materials with such non-trivial bands hinders future studies.

Motivated by earlier studies, we investigate the surface electronic structure of VSe₂ TMD grown on the surface of Bi₂Se₃ TI and show the emergence of a flat band in the electronic states at low VSe₂ coverage level. This flat band covers the entire $k_x - k_y$ plane of the Brillouin zone (BZ) and it displays dispersionless along the k_z direction as well. Furthermore, our circular dichroism ARPES (CD-ARPES) measurements revealed that the CD signal of the flat band reverses the sign at several points within the BZ. Another notable observation is that VSe₂ growth and emergence of the flat band do not reshape the Dirac cone of Bi₂Se₃ in the vicinity of the DP unlike the case of transition metal doping which opens a large gap at the DP²⁶. We also observed Moiré patterns in VSe₂ domains of monolayer (ML) thickness and stripe type patterns in bare Bi₂Se₃ through scanning tunneling microscopy (STM). Along with these observations, electron doping impact on the band structure of the system suggests that the flat band might be due to the Mott insulator like interaction correlated with the charge density wave (CDW) phase. To further shed light on the crystalline and chemical properties of the system, scanning transmission electron microscopy (STEM), micro-spot low energy electron diffraction (μ LEED), and x-ray photoemission spectroscopy (XPS) experiments were conducted. Our results demonstrate rich physics and suggest a large family of materials of possible emergent flat bands and thus will motivate future

studies on materials with superconductivity at high-temperatures, QSL states, or FQHE by using our approach.

Structural characterization: Bi_2Se_3 and VSe_2 crystals are layered materials with their atomic stacking geometry shown in Fig. 1a. The layers in each compound are separated by so-called van der Waals (vdW) gaps with weak covalent out-of-plane bonds connecting the layers. This is the reason that $\text{VSe}_2 / \text{Bi}_2\text{Se}_3$ heterostructure can be grown despite the large in-plane lattice mismatch of around 20 % between the two materials²⁷⁻²⁸. Figs. 1b and 1c depict the relevant core-levels of such structures formed by the growth of 0.3 ML and 3 ML VSe_2 on 12 quintuple layer (QL) Bi_2Se_3 . Upon deposition of the VSe_2 , the spectral shape of the Bi 5d peaks of Bi_2Se_3 does not exhibit a prominent modification indicating the absence of V metals at the interface and/or in the bulk (Fig. 1b)²⁹. Compared with pristine Bi_2Se_3 , the Se 3d peak, however, appears at 0.1 eV higher binding energy upon VSe_2 deposition. This can be better seen in the inset of Fig. 1b displaying the scaled Se 3d peaks to the same height. The difference in binding energy could be due to the CDW phase of VSe_2 ²⁷. V $2p_{1/2}$ and $2p_{3/2}$ peaks shown in Fig. 1c are located at 513 eV and 520.6 eV binding energies, being in agreement with recent reports²⁸.

To further explore the system, we show a high-angle annular dark-field (HAADF)-STEM cross-section image of 3 ML $\text{VSe}_2 / 12$ QL Bi_2Se_3 heterostructure in Fig. 1d. Bi_2Se_3 and VSe_2 exhibit regular atomic layers with smooth interfaces and vdW gaps marked with red arrows in Fig. 1d. On the other hand, the STEM data does not exhibit a clear interface spacing between the VSe_2 and Bi_2Se_3 which could strongly modify the local electronic structure. Furthermore, the STEM energy dispersive X-ray spectroscopy elemental maps presented in Fig. S1 (supplementary materials) shows the atomic distribution of Bi in the Bi_2Se_3 layers, V in VSe_2 layers, and Se across the heterostructure as expected.

Fig. 1e and 1f show the STM image of Bi_2Se_3 and VSe_2 regions of a 0.3 ML VSe_2 / 12 QL Bi_2Se_3 sample, respectively. The Bi_2Se_3 surface has a stripe-like pattern similar to Cs and Fe doped Bi_2Se_3 ³⁰. The STM image of the VSe_2 domains presented in Fig. 1f exhibits a Moiré pattern with $\sim 2 \text{ nm} \times 2 \text{ nm}$ superstructure. This differs from the previous studies conducted on VSe_2 / graphene in which such superstructure formation was absent²⁷. Moiré pattern can be formed by a small misfit between the in-plane lattice parameters of the film and the underlying material or the relative rotation of two layers to each other, or both. By contrast, the lattice mismatch between the VSe_2 and Bi_2Se_3 is quite large (about 20 %). Unfortunately, we cannot make a quantitative analysis for precise determination of the in plane lattice parameters or the atomic displacement due to the limitation in our STM data taken at room temperature experiment. But, similar Moiré pattern formation is also observed on monolayer MoSe_2 grown on a graphene substrate whose origin is attributed to the lattice mismatch between the multiple unit cells of the two materials³¹. Thereby, the Moiré pattern in VSe_2 could be formed due to the small mismatch between four-five-unit cells of Bi_2Se_3 ($4a_{\text{BS}} = 16.56 \text{ \AA}$ or $5a_{\text{BS}} = 20.7 \text{ \AA}$) and five-unit cells of VSe_2 ($5a_{\text{VS}} = 16.8 \text{ \AA}$ or $6a_{\text{VS}} = 20.16 \text{ \AA}$) for the rotationally aligned lattice geometry. Alternatively, the Moiré pattern could form be formed by the rotational misalignments of Bi_2Se_3 and VSe_2 atomic lattices. Moreover, the details of the STM data reveal that the layer heights are 6.8 \AA for VSe_2 and 9.6 \AA Bi_2Se_3 (Fig. S2, supplementary materials), which is in agreement with published results³².

ARPES electronic structure: To examine the band structure, the binding energy versus k_y plots are given for 12 QL Bi_2Se_3 in Fig. 2a and for 0.3 ML VSe_2 / 12 QL Bi_2Se_3 in Fig. 2b. The Bi_2Se_3 sample exhibits the typical band structure with the linear Dirac surface states (DSSs) forming the Dirac cone with the Dirac point (DP) at 0.36 eV below E_{F} ³³. Upon deposition of 0.3 ML VSe_2 on Bi_2Se_3 , a flat band with 0.47 eV binding energy and $\sim 0.18 \text{ eV}$ bandwidth emerges in the surface

electronic structure (Fig. 2b). The flatness of the band is well distinguished in the energy distribution curves (EDCs) shown in Fig. 2c. The bulk bands and the DSS of Bi_2Se_3 strongly disperse as a function of k_y , while the flat band retains dispersionless across the $\bar{\Gamma} - \bar{M}$ high symmetry lines. VSe_2 growth also induces the well-known M-state quantization³⁴ of the bulk valance band (BVB) of Bi_2Se_3 shown in Fig. 2b. Moreover, the flat band overlaps with the lower branch of the Dirac cone in the vicinity of $k_y = 0 \text{ \AA}^{-1}$ without inducing a prominent change in its spectral shape. This can be even better seen in the films with larger VSe_2 coverage confirming that the flat band, DSSs, and the dispersive V 3d state of VSe_2 coexist in the surface electronic structure (Fig. S3, supplementary materials). Also, ARPES data for the thicker VSe_2 coverage suggests that the flat band is localized on the bare Bi_2Se_3 and/or at the interface between VSe_2 and Bi_2Se_3 (Fig. S4, supplementary materials). We should also note that 0.3 ML VSe_2 / 12 QL Bi_2Se_3 sample shows an insulating gap at the E_F which will be discussed in the following sections of the text.

To further investigate the flat band, a $k_x - k_y$ intensity plot at E_F and the binding energy of the flat band (E_{FB}) are shown in Fig. 2d and in Fig. 2e, respectively. The Fermi surface is dominated by a circular counter of the DSSs centered at $\bar{\Gamma}$ point. The constant energy cut at E_{FB} reveals another remarkable feature, namely that the flat band reaches beyond the \bar{M} and \bar{K} points in the BZ. This observation reveals that the flat band fills the entire BZs of Bi_2Se_3 and VSe_2 as depicted by black and red hexagons in Fig. 2e, respectively. Such electronic state spread over large momentum area can significantly enhance the electronic correlation yielding quantum effects at very high-temperatures. It is also worth noting that the LEED pattern of the sample shows rotationally stretched diffraction spots along the rotational direction indicating the presence of the rotationally misaligned VSe_2 domains (Fig. S2a, supplementary materials) with respect to each other and to the Bi_2Se_3 substrate. The rotational misfit of $\pm 3^\circ$ estimated from μLEED pattern, however, is too

small for a band to span whole BZ and to induce a fully occupied constant energy counter in the momentum map.

Photon energy-dependent ARPES: In ARPES experiments, changing the photon energy corresponds to mapping the electronic states along the k_z direction of the BZ. By recording the electronic structure with a wide photon energy range, a k_{\parallel} vs. k_z or binding energy vs. k_z dispersions can be also extracted. This method allows studying the energy bands along the k_z (ou-of-plane) direction to distinguish the non-dispersive states from the dispersive bulk bands. Such spectra acquired at varying photon energies (40 eV to 70 eV) for 0.3 ML VSe₂ / 12 QL Bi₂Se₃ sample are given in Fig. 3. In the plot of k_z versus k_y dispersion at E_F , DSSs marked with dashed red lines exhibit no k_z dependence (Fig. 3a). Similar spectrum at E_{FB} given in Fig. 3b shows that a high spectral intensity along the $k_y = 0 \text{ \AA}^{-1}$ originates from the bottom of the Dirac cone of Bi₂Se₃. Away from the $k_y = 0 \text{ \AA}^{-1}$, the plot has non-vanishing spectral intensity contributed by the flat band. This can be better seen in the momentum distribution curves (MDCs) obtained at various k_z points (Fig. 3c) in which each spectrum exhibits always finite density of states along the k_y momentum direction. This implies the dispersionless nature of the flat band along the k_z momentum direction. To further validate this observation, we show the binding energy - k_z plots along the $k_y = \pm 0.3 \text{ \AA}^{-1}$ directions in Fig. 3d and 3e, respectively. The plots clearly show that the flat band at 0.47 eV binding energy is k_z - independent confirming its non-bulk derived nature. We should also note that the M-shape bulk band located at 1 eV binding energy exhibits a nearly non-dispersive feature along the k_z as shown in Fig. 3d and 3e. To further reveal the details of the flat band, Fig 3f depicts the EDCs taken at different k_z points. One can see that the EDC of the flat band does not exhibit a k_z dependent evolution in the binding energy and bandwidth providing a signature that the flat band originates from a single band.

CD-ARPES: Circular dichroism (CD)-ARPES has gained great attention due to its feasibility to investigate the helical spin-orbit texture in topological surface states³⁵. The principle of the method is the spectral weight differences in ARPES arising from the opposite helicity of the circularly polarized light. CD-ARPES is then obtained from $[(I_{\text{RCP}} - I_{\text{LCP}})]/[(I_{\text{RCP}} + I_{\text{LCP}})]$ where I_{RHP} and I_{LHP} are photoemission intensities for RCP and LCP lights, respectively. Thus, we have recorded the band structure of 0.3 ML VSe₂ / 12 QL Bi₂Se₃ sample with RCP and LCP, shown in Fig. 4a and in Fig. 4b, respectively. The corresponding CD-ARPES is presented in Fig. 4c with red (negative-CD) and blue (positive-CD) color representations. The bulk bands of Bi₂Se₃ dispersing below 0.8 eV binding energy show a strong DC as seen in Fig. 4a-4c. CD from the DSSs of Bi₂Se₃ is also seen switching the spectral weight from the $-k_y$ to $+k_y$ regions when changing the excitation from RCP to LCP. For clarity, the DC signal versus k_y is plotted in Fig. 4d at 0.1 eV binding energy in which the CD is positive for left and negative for the right side of the Dirac cone, marked with vertical arrows. Further away from the $k_y = 0 \text{ \AA}^{-1}$, the plot in Fig. 4d still shows non-zero CD. This is likely originating from the V 3d orbitals which dominate the E_F density of states in VSe₂²⁷. Also, since the spectra are conducted with 50 eV photons corresponding to nearly Z-point of the BZ, the BCBs of Bi₂Se₃ do not contribute to ARPES spectra in the vicinity of the E_F as seen in Fig. 2a.

To investigate the dichroism effect in the flat band, the CD at E_{FB} is plotted as a function of k_y in Fig. 4e and it exhibits sign inversions at $k_y = 0 \text{ \AA}^{-1}$ and $k_y = \pm 0.5 \text{ \AA}^{-1}$ and the maxima at $k_y = \pm 0.25 \text{ \AA}^{-1}$. Similar to the DSSs, the CD in the flat band also exhibits helical-texture where opposite k_y momentums have opposite signs of the CD. Notably, zero CD signal is also observed as white color in the CD-ARPES along the $k_y = 0 \text{ \AA}^{-1}$. This depicts the nodal line which was proposed to be the characteristic feature of the 2D electronic structure³⁶. In particular, the CD signal of the

DSSs depends on the incident photon energy assigning it to the final state effect in the photoemission process³⁵. This was discussed in Ref 36 with details where they propose the non-trivial connection between the spin orbit texture and the CD signal. Thereby, the helical CD texture and the nodal line band suggest that the flat band could be also topologically non-trivial.

Electron doping impact on the band structure: Tuning the chemical potential in the strongly correlated systems induces a mass renormalization. This has been seen in superconductors as the mass enhancement referring to the flattening of the bands³⁷⁻³⁸ and also exists in the CDW phase of the excitonic insulators³⁹. Also, this mechanism usually coexists with a metal-insulator transition in superconductors³⁷. Likewise, the dispersion of the flat band could be controlled through the electron or hole doping. However, in our case, since the flat band is already dispersionless, so the mass normalization could be expected. Namely, the flat band can gain weak dispersion upon the tuning of the E_F . To test this idea and to probe the possible unoccupied bands above the Fermi level, we studied the band structure of the sample under the surface deposition of potassium (K) where we found further spectroscopic anomalies in 0.3 ML VSe_2 / 12 QL Bi_2Se_3 sample (Fig. 5). The first notable observation is that K deposition induces a pair of quantum well states (QWS) shown with black arrows in Fig. 5b. This proves the electron doping induced band bending in the BVB of Bi_2Se_3 . More interestingly, the leading edge shifts with K doping revealing an 0.08 eV insulating gap at the E_F (Fig. 5a-5b). The shift is more obvious in the integrated EDCs (Fig. 5c) where sharp edges are observed at different energies before and after K deposition. This indicates that the gap closing is not due to the broadening or the formation of an additional spectral feature in the vicinity of the E_F . EDCs along the k_R and k_L momentums where the DSSs cut the E_F (Fig. 5a) also exhibit the same insulating gap as shown in Fig. 5e and 5f. This shows that not only VSe_2 but also bare Bi_2Se_3 regions have an insulating gap at the E_F since the size of x-ray beam spot on

the sample is considerably larger than the size of individual VSe₂ domains. This argument is also supported by the absence of the multiple Dirac cones which are expected to be located at the bare and the VSe₂ covered parts of Bi₂Se₃ layers. These realizations show that the flat band could be originating from Bi₂Se₃ when modified by VSe₂ sublayer. Another peculiar anomaly is the difference of binding energy shifts of bulk bands, DSS, and the flat band, induced by the K deposition. While Bi₂Se₃ bulk and Dirac states exhibit the expected electron doping, the flat band shows negative electron compressibility. The flat band binding energy changes from 0.47 eV before K doping to a lower value of 0.33 eV after K doping. On the other hand, the binding energy of the DP shifts from 0.36 eV to 0.55 eV. Similar band bending towards higher binding energy is also seen in the bulk bands of Bi₂Se₃ (Fig. 5a-5b). (Note that the binding energies are given with respect to the highest occupied states in the ARPES map shown in Fig. 5b.) The existence of opposite energy shifts of the flat band and Dirac bands opens up a pathway to tune both, the binding energy of the DP as well as the flat band with respect to each other. If hole doping of Bi₂Se₃ i. e. via Ca substitution⁴⁰, was to be included, both DP and the flat band could be tuned to E_F which might yield exotic transport properties. Hence, we have demonstrated the presence of a possibly unique tuning parameter for the transport properties of such low dimensional topological system.

We should also point out that the ARPES data of the K doped sample in Fig. 5b shows minute dispersion of the flat band, an apparent decrease of its binding energy when approaching the $\bar{\Gamma}$ point. However, this dispersion is too small for a precise detection but might be related to the modification of the CDW phase³⁹. Our fittings of the EDCs at different k_y momenta (not shown) yield the energy dispersion to be about 35 meV between $k_y = 0.15 \text{ \AA}^{-1}$ and $k_y = 0.6 \text{ \AA}^{-1}$ momentum points. This effect might be further enhanced by tuning the chemical potential of the system which opens an opportunity for future studies. Nevertheless, the insulating gap and the mass

normalization with the electron doping, even if it is small, suggest that the flat band could be related to strong electron correlation effects.

Discussion: Dispersionless flat bands can be explained by several mechanisms. V 3d derived magnetic impurity bands are the first mechanism to be considered as the spectroscopic origin of the flat band⁴¹. However, our core level spectra and STM data do not show any signature of isolated atoms. Also, our photon energy dependent ARPES and the rather complex CD-ARPES spectra indicate that the flat band should be considered to have non-trivial origin.

Another scenario to consider would be the existence of superlattices as seen in $\sqrt{3} \times \sqrt{3}$ silicene superstructure by STS in which the local density of states forms the electronic Kagome lattice⁴². The interface dislocation or the strain can also flatten the original bands by introducing pseudo-magnetic field term to the Hamiltonian in Moiré superstructures⁴. However, a pronounced band flattening in this scenario requires superstructure patterns with at least a few tens of nanometers periodicity which is much larger than one observed in the present case. Furthermore, the flat bands discussed within the superlattice frameworks are dispersionless only in the BZ of the superstructure which is smaller than the BZ corresponding to the unitcell^{25, 42}. This mechanism gives rise to a dispersionless flat band within a small momentum window. On the other hand, the flat band reported here does not shrink into the BZ of the Moiré or the stripe pattern superstructures and it is robust against electron doping. Therefore, although we cannot entirely exclude that the flat band electronic state in VSe₂ / Bi₂Se₃ may be related to the atomic superstructures, there are other possibilities to consider^{23-25, 42}.

Dispersionless flat bands with an insulating gap at the E_F indicate to strong electronic correlation. This could be explained by considering the Mott insulator or charge-transfer insulating states which are generally in proximity to CDW phases¹⁶. Indeed, the presence of corrugated bright and

dark Bi_2Se_3 domains in the STM image (Fig. 1e) supports the persistence of the CDW phase in agreement with earlier studies⁴³⁻⁴⁴. In the Mott phase, a strong Coulomb repulsion splits d- or f-bands into the lower (occupied) and upper (unoccupied) Hubbard bands (LHB and UHB) which are separated with an insulating gap located in the vicinity of E_F ¹⁶. The insulating gap in the Mott insulator correlated with the CDW phase strongly depends on the chemical potential of the system¹⁵. Thus, the chemical potential could shrink the gap by shifting the LHB and UHB closer to the E_F and each other. In this scenario, the Hubbard bands could exhibit opposite energy shifts than other bands upon doping¹⁵⁻¹⁶. Similarly, a large Hubbard interaction could induce an antiferromagnetic order and open an energy gap at E_F in a topological honeycomb lattice⁴⁵. Furthermore, p-type Hubbard bands with an insulating ground state were also predicted in Bi_2Se_3 and $\text{Bi}_2\text{Te}_2\text{Se}$ upon enhancing the Coulomb repulsion¹⁹⁻²¹. The similarities between the Mott insulators and the $\text{VSe}_2 / \text{Bi}_2\text{Se}_3$ could suggest that the flat band in our sample could be formed by the strong correlation effects.

On the other hand, up to the date, the surface electronic structure of TIs has been studied by ARPES under the deposition of various magnetic and non-magnetic elements, and none of the approaches revealed the flat band spectral feature⁴⁶. This controversy could be related to the location of the dopants in the crystal. The elemental dopants occupy the vdW gap or the sublattice sites in the bulk⁴⁷, while VSe_2 domains are located on the surface of Bi_2Se_3 . Therefore, the magnetic properties of the VSe_2 could also play a vital role in the formation of the distinct electronic states on the surface of Bi_2Se_3 without modifying its bulk band topology⁴⁸. Nevertheless, the details of the flat band electronic structure with a realistic scenario are more complicated since non-trivial band topology and the strong spin-orbit coupling are also expected to play a role in the evolution of the electronic structure. The complete understanding of the physics behind the flat band and the

insulating gap requires a broad and elaborate theoretical and experimental efforts. As a first example of the dispersionless electronic excitation in a topologically non-trivial band structure, our results could open a new pathway in the critical field of experimental realization and control of novel quantum effects and new states of the matters.

Methods:

Material preparation: Molecular beam epitaxial growth (MBE) technique was employed to grow VSe_2 / Bi_2Se_3 and Bi_2Se_3 samples in a custom ultra-high vacuum system located at the ESM beamline of NSLS-II. 5N Se and Bi sources were evaporated from the ceramic crucibles while the e-beam evaporation method was used for V (99.8% purity) source. All samples were grown on $Al_2O_3(0001)$ substrates at 255 °C. Before the growth, the substrates were first degassed at 550 °C for three hours and flashed at 850 °C for 5 min. Sample thicknesses were estimated within a 15 % error bar by using a quartz thickness monitor and x-ray photoemission spectroscopy. Samples for ARPES and μ LEED experiments were capped with 20 nm amorphous Se film before being removed from the MBE chamber.

XPS: Core-levels were recorded with 1486.7 eV non-monochromated x-ray source at room temperature with a vacuum interlocked MBE-photoemission system at the surface science laboratory of the Department of Physics of the University of Connecticut. Core-level binding energies were determined with an error of 0.1 eV.

ARPES: ARPES experiments were performed at 21-ID-1 ESM beamline of National Synchrotron Light Source II (NSLS-II) by using a DA30 Scienta electron spectrometer. The pressure in the photoemission chamber was 1×10^{-10} Torr and samples were kept at 15 K during the experiment by a closed-cycle He cryostat. The energy resolution in the ARPES experiments was better than

15meV with a spot size of $\sim 20 \mu\text{m}$. Before the ARPES experiments, samples were annealed at 220 °C for 30 minutes to remove the Se capping layer. The angle between the light and the surface normal of the sample is 55° at the normal emission during the ARPES experiments. The films were grounded with a tantalum clip. A part of the ARPES experiments was conducted at the linear undulator beamline at the Hiroshima Synchrotron Radiation Center (HiSOR) BL-1 [S1]. Photon energy is converted to k_z momentum space by using the free electron final state approximation $\hbar k_z = \sqrt{2m_e(E_{\text{kin}} \cos^2\theta + V_0)}$ where m_e is the free electron mass, E_{kin} is the kinetic energy of a photoelectron, and V_0 is the inner potential which is 11.8 eV for Bi_2Se_3 [S2].

TEM and STM: HAADF-STEM images were acquired with Hitachi HD2700C dedicated STEM with a probe Cs corrector operating at 200 kV at room temperature. Samples were prepared using the in-situ lift-out method on the FEI Helios 600 Nanolab dual-beam FIB. Final milling was completed at 2 keV. Scanning tunneling microscope (Omicron VT- STM -XA 650) experiments were performed in an ultrahigh vacuum (UHV) system with a base pressure of 2×10^{-10} Torr at room temperature. All the STM images were observed in constant current mode using Pt/ Ir tips. All bias values in the text refer to the bias applied to the sample. The STM images were analyzed using Gwyddion-2.55 software package. HAADF-STEM and STM experiments were conducted at the Center for Functional Nanomaterials, Brookhaven National Laboratory. Samples for STM were transferred with a vacuum suitcase.

LEED: μLEED experiment was performed at XPEEM/LEEM endstation of the ESM beamline (21-ID-2).

Acknowledgment: This research used ESM (21-ID-1, 21-ID-2) beamline of the National Synchrotron Light Source II, a U.S. Department of Energy (DOE) Office of Science User Facility

operated for the DOE Office of Science by Brookhaven National Laboratory under Contract No. DE-SC0012704. This work also used the resources of the Center for Functional Nanomaterials, Brookhaven National Laboratory, which is supported by the U.S. Department of Energy, Office of Basic Energy Sciences, under Contract No. DE-SC0012704. ARPES experiments in Hiroshima were performed with the approval of program advisory committee of HISOR) Proposal No. 19BG041). Author T. Y. would like to thank Prof. A. V. Balatsky for useful discussions.

Author Contributions: T.Y conceived and designed the experiments. T.Y prepared the samples and performed the photoemission experiments with K. K., E. V, and B. S's help. E. F. S. performed the ARPES experiments at HISOR. X. T. conducted the STM measurements. Z.D. and J. T. S. performed μ LEED measurements. S. H. and K. K. performed HAADF-STEM experiments. T. Y analyzed the experimental results and wrote the manuscript with contribution from E. F.S., B. S., K. K., and E. V.

Competing interests: The authors declare that they have no competing interests.

References

1. Heikkilä, T. & Volovik, G. E. Flat bands as a route to high-temperature superconductivity in graphite, 123–144 (Esquinazi, P. (ed.), (Springer International Publishing AG Switzerland, 2016).
2. Cao, Y. et al. Unconventional superconductivity in magic-angle graphene superlattices. *Nature* **556**, 43–50 (2018).
3. Heikkilä, T. T., Kopnin, N. B. & Volovik, G. E. Flat bands in topological media. *JETP Lett.* **94**, 233–239 (2011).

4. Tang, E. & Fu, L. Strain-induced partially flat band, helical snake states and interface superconductivity in topological crystalline insulators. *Nat. Phys.* **10**, 964969 (2014).
5. E. Tang, J. W. Mei, X. G. Wen, High-temperature fractional quantum Hall states. *Phys. Rev. Lett.* **106**, 236802 (2011).
6. Sun, K., Gu, Z., Katsura, H. & Das Sarma, S. Nearly flatbands with nontrivial topology. *Phys. Rev. Lett.* **106**, 236803 (2011).
7. Guo, H. M. & Franz, M. Topological insulator on the kagome lattice. *Phys. Rev. B* **80**, 113102 (2009).
8. Lin, Z. et al. Flatbands and emergent ferromagnetic ordering in Fe₃Sn₂ kagome lattices. *Phys. Rev. Lett.* **121**, 96401 (2018).
9. Kang, M. et al. Dirac fermions and flat bands in the ideal Kagome metal FeSn. *Nat. Mater.* **19**, 163–169 (2020).
10. Yin, J. X. et al. Negative flat band magnetism in a spin–orbit-coupled correlated kagome magnet. *Nat. Phys.* **15**, 443–448 (2019).
11. Kopnin, N. B., Heikkilä, T. T. & Volovik, G. E. High-temperature surface superconductivity in topological flat-band systems. *Phys. Rev. B* **83**, 220503(R) (2011).
12. Kopnin, N. B., Ijäs, M., Harju, A. & Heikkilä, T. T. High-temperature surface superconductivity in rhombohedral graphite. *Phys. Rev. B* **87**, 140503 (2013).
13. Marchenko, D. et al. Extremely flat band in bilayer graphene. *Sci. Adv.* **4**, 11 (2018).
14. Volovik, G. E. Graphite, graphene and the flat band superconductivity. *JETP Letters* **107**, 516–517 (2018).
15. Qiao, S. et al. Mottness collapse in 1T-TaS_{2-x}Se_x transition-metal dichalcogenide: an interplay between localized and itinerant orbitals. *Phys. Rev. X* **7**, 041054 (2017).

16. Ang, R. et al. Superconductivity and bandwidth-controlled Mott metal–insulator transition in 1T-TaS_{2-x}Se_x. *Phys. Rev. B* **88**, 115145 (2013).
17. Pasquier, D. & Yazyev, O.V. Charge density wave phase, Mottness, and ferromagnetism in monolayer 1T–NbSe₂. *Phys. Rev. B* **98**, 045114 (2018).
18. Tresca, C. & Calandra, M. Charge density wave and spin 1/2 insulating state in single layer 1T–NbS₂. *2D Materials* **6**, 035041 (2019).
19. Craco, L. & Leoni, S. Bulk quantum correlations and doping-induced nonmetallicity in the Bi₂Se₃ topological insulator. *Phys. Rev. B* **85**, 075114 (2012).
20. Liu, M. et al. Electron interaction-driven insulating ground state in Bi₂Se₃ topological insulators in the two-dimensional limit. *Phys. Rev. B* **83**, 165440 (2011).
21. Craco, L. & Leoni, S. Tunable Kondo-Mott physics in bulk Bi₂Te₂Se topological insulator. *Phys. Rev. B* **85**, 195124 (2012).
22. Chen, G. et al. Evidence of a gate-tunable Mott insulator in trilayer graphene moiré superlattice. *Nat. Phys.* **15**, 237–241 (2019).
23. Wu, F., Lovorn, T., Tutuc, E. & MacDonald, A. H. Hubbard model physics in transition metal dichalcogenide moiré bands. *Phys. Rev. Lett.* **121**, 026402 (2018).
24. Naik, M. H. & Jain, M. Ultraflatbands and shear solitons in moiré patterns of twisted bilayer transition metal dichalcogenides. *Phys. Rev. Lett.* **121**, 266401 (2018).
25. Bi, Z., Yuan, N. F. Q. & Fu, L. Designing flat bands by strain. *Phys. Rev. B* **100**, 035448 (2019).
26. Yilmaz, T. et al. Distinct Effects of Cr Bulk Doping and Surface Deposition on the Chemical Environment and Electronic Structure of the Topological Insulator Bi₂Se₃. *Appl. Surf. Sci.* **407**, 371–378 (2017).

27. Chen, P. et al. Unique Gap Structure and Symmetry of the Charge Density Wave in Single-Layer VSe₂. *Phys. Rev. Lett.* **121**, 196402 (2018).
28. Liu, Z. L. et al. Epitaxially grown monolayer VSe₂ An air-stable magnetic two-dimensional material with low work function at edges. *Sci. Bull.* **63**, 419 (2018).
29. L.A. Walsh, L. A. et al. Interface Chemistry of Contact Metals and Ferromagnets on the Topological Insulator Bi₂Se₃, *Jour. of Phys. Chem. C* **121**, 23551 (2017).
30. Shokri, R. Coexistence of impurity-induced quasi-one-dimensional electronic structure and topological surface states of Bi₂Se₃. *J. Appl. Phys.* **119**, 085304 (2016).
31. Ugeda, M. M. et al. Giant bandgap renormalization and excitonic effects in a monolayer transition metal dichalcogenide semiconductor. *Nature Mater.* **13**, 1091–1095 (2014).
32. Duvjir, G. et al. Emergence of a Metal–Insulator Transition and High-Temperature Charge-Density Waves in VSe₂ at the Monolayer Limit. *Nano Lett.* **18**, 5432–5438 (2018).
33. Xia, Y. et al. Observation of a large-gap topological-insulator class with a single Dirac cone on the surface. *Nat. Phys.* **5**, 398 (2009).
34. Bianchi M., Hatch R. C., Mi J., Iversen B. B. & Hofmann P. Simultaneous quantization of bulk conduction and valence states through adsorption of nonmagnetic impurities on Bi₂Se₃. *Phys. Rev. Lett.* **107**, 086802 (2011).
35. Wang, Y. & Gedik, N. Circular dichroism in angle-resolved photoemission spectroscopy of topological insulators. *Phys. Status Solidi* **7**, 64–71 (2013).
36. Scholz, M. R. et al. Reversal of the circular dichroism in angle-resolved photoemission from Bi₂Te₃. *Phys. Rev. Lett.* **110**, 216801 (2013).
37. Wang, Z, Tsurkan, V., Schmidt, M., Loidl, A. & Deisenhofer, J. Tuning orbital-selective correlation effects in superconducting Rb_{0.75}Fe_{1.6}Se_{2-z}S_z. *Phys. Rev. B* **93**, 104522 (2016).

38. Yoshida, T. et al. Direct observation of the mass renormalization in SrVO₃ by angle resolved photoemission spectroscopy. *Phys. Rev. Lett.* **95**, 146404 (2005).
39. Fukutani, K. et al. Electrical Tuning of the Excitonic Insulator Ground State of Ta₂NiSe₅. *Rev. Lett.* **123**, 206401 (2019).
40. Hor, Y. S. et al. p-type Bi₂Se₃ for topological insulator and low-temperature thermoelectric applications. *Phys. Rev. B* **79**, 195208 (2009).
41. Feng, L. et al. Flat bands near Fermi level of topological line defects on graphite. *Appl. Phys. Lett.* **101**, 113113 (2012).
42. Li, Z. et al. Realization of flat band with possible nontrivial topology in electronic Kagome lattice. *Sci. Adv.* **4**, eaau4511 (2018).
43. Chen, K. P., Chung, F. R., Wang, M. & Koski, K. J. Dual element intercalation into 2d layered Bi₂Se₃ nanoribbons. *J. Am. Chem. Soc.* **137**, 5431–5437 (2015).
44. Koski, K. J. et al. Chemical intercalation of zerovalent metals into 2D layered Bi₂Se₃ nanoribbons. *JACS* **134**, 13773–13779 (2012).
45. Raghu, S., Qi, X. L., Honerkamp, C. & Zhang, S.-C. Topological Mott insulators. *Phys. Rev. Lett.* **100**, 156401 (2008).
46. Valla, T., Pan, Z. H., Gardner, D., Lee, Y. S. & Chu, S. Photoemission spectroscopy of magnetic and nonmagnetic impurities on the surface of the Bi₂Se₃ topological insulator. *Phys. Rev. Lett.* **108**, 117601 (2012).
47. Abdalla, L. B., Seixas, L., Schmidt, T. M., Miwa, R. H. & Fazzio, A. Topological insulator Bi₂Se₃(111) surface doped with transition metals: an ab-initio investigation. *Phys. Rev. B* **88**, 045312 (2013).

48. Bonilla, M. et al. Strong room-temperature ferromagnetism in VSe₂ monolayers on van der Waals substrates. *Nat. Nanotechnol.* **13**, 289–293 (2018).

Figures:

Fig. 1 | Structural characterization. **a**, Top and side views of Bi₂Se₃ and VSe₂ crystal structures. Hexagonal BZs with the high-symmetry points are given in the lower part of **a**. **b**, Core-level photoemission spectra of Bi 5d and Se 3d obtained from 12 QL Bi₂Se₃, 0.3 ML VSe₂ / 12 QL Bi₂Se₃, and 3 ML VSe₂ / 12 QL Bi₂Se₃ samples. The inset in **b** shows the Se 3d peaks for pristine and 3 ML VSe₂ covered Bi₂Se₃ after scaling peaks to the same height for visual comparison. **c**, V 2p core levels for 0.3 ML VSe₂ / 12 QL Bi₂Se₃ and 3 ML VSe₂ / 12 QL Bi₂Se₃ samples. The atomic stoichiometry of Se to V is computed to be 2 by using the peak areas and photoionization cross-sections. **d**, HAADF-STEM cross-section image of 3 ML VSe₂ / 12 QL Bi₂Se₃ heterostructure. The color contrast in **d** is correlated with the atomic number (Z-contrast). **e, f**, Room temperature STM images of Bi₂Se₃ (at sample bias 100 mV, set point 1 nA) and VSe₂ (at sample bias 80 mV, set point 1 nA) surfaces, respectively obtained from 0.3 ML VSe₂ / 12 QL Bi₂Se₃. Yellow parallelogram in **f** represents the Moiré unit cell.

Fig. 2 | Emergence of the flat band revealed by ARPES. **a-b**, Experimental electronic structures of 12 QL Bi₂Se₃ and 0.3 ML VSe₂ / 12 QL Bi₂Se₃ samples, respectively. Spectra were collected with 50 eV linear horizontal polarized lights. BVB refers to the bulk valance band of Bi₂Se₃. **c**, Momentum integrated EDCs of 0.3 ML VSe₂ / 12 QL Bi₂Se₃ acquired with 110 eV photon energy along the $\bar{\Gamma}$ - \bar{M} direction in the BZ. **d-e**, Constant energy counters at the E_F and the E_{FB}, respectively for 0.3 ML VSe₂ / 12 QL Bi₂Se₃. Red and black hexagons in **e** correspond to the BZ of VSe₂ and Bi₂Se₃, respectively. In-plane lattice parameters of 4.14 Å for Bi₂Se₃ and 3.356 Å for VSe₂ were employed to compute the BZs^{27, 31}.

Fig. 3 | Photon energy-dependent ARPES experiment. **a-b**, $k_y - k_z$ dispersions at the E_F and the E_{FB} , respectively. Dashed red lines in **a** mark the DSSs. **c**, MDCs at different k_z points **d-e**, Binding energy versus k_z maps at $k_y = \pm 0.3 \text{ \AA}$, respectively. Dashed cyan colored lines in **d** and **e** represent the modulation of the flat band along the k_z direction. **f**, EDCs at various k_z points to study the spectral shape of the flat band. ARPES maps for the plots were conducted along the $\bar{\Gamma}-\bar{M}$ direction in the BZ.

Fig. 4 | CD-ARPES. **a-b**, ARPES maps of 0.3 ML VSe₂ / 12 QL Bi₂Se₃ sample recorded with RCP and LCP lights, respectively. **c**, Computed CD-ARPES. **d-e**, CDs as a function of k_y at 0.1 eV binding energy and the E_{FB} , respectively.

Fig. 5 | Electron doping impact on the band structure. **a-b**, ARPES maps of 0.3 ML VSe₂ / 12 QL Bi₂Se₃ before (bare) and after K-doping, respectively. Spectra were obtained with 50 eV photons at 15 K. **c-f** present integrated EDC within $k_y = \pm 0.6 \text{ \AA}$ and EDCs along the k_0 , k_R , and k_L momentums as marked in **a**. In **a-b**, dashed lines show the energy shifts of the different bands as specified in the figures and the yellow solid line indicates the leading edge. In **c-f**, green, pink, black, brown vertical lines represent the binding energy of the flat band, leading edge, bulk bands, and the DP, respectively. The arrows in **c-f** point the direction of the energy shifts.

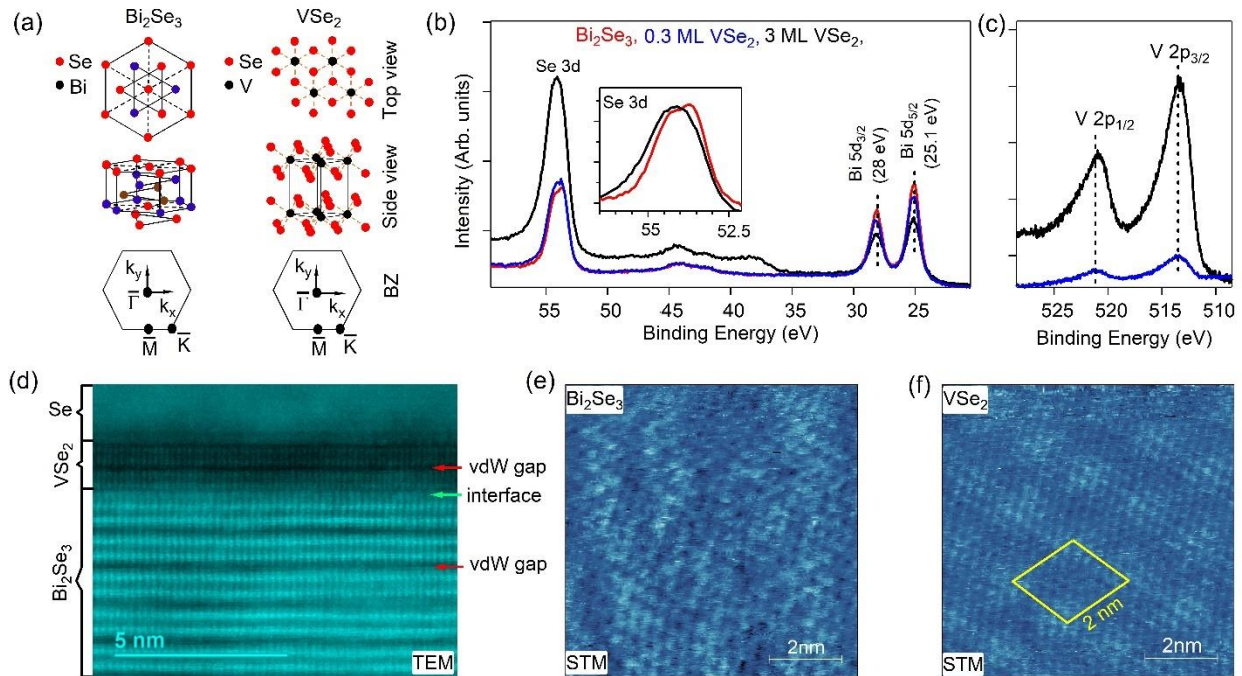


Fig. 1

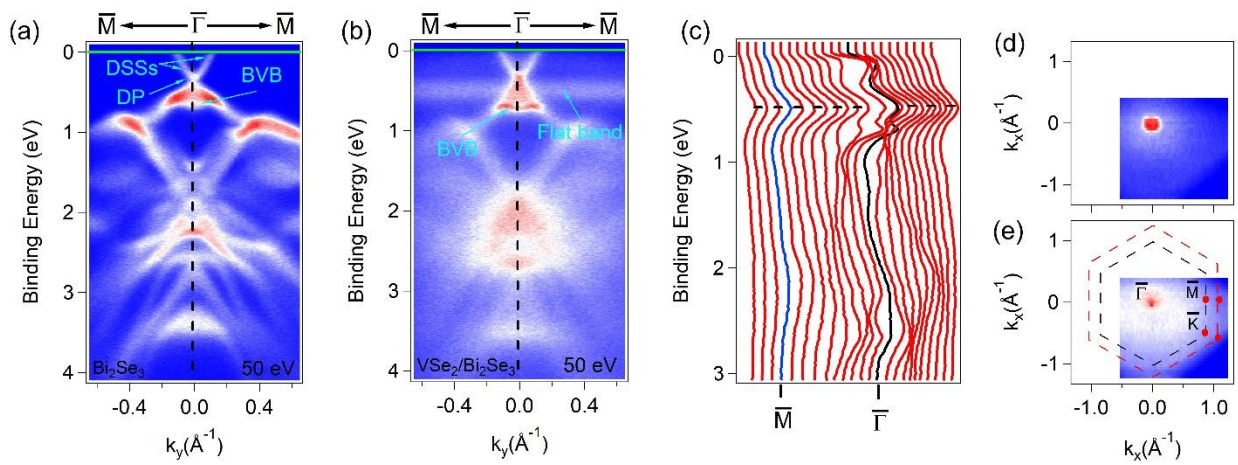


Fig. 2

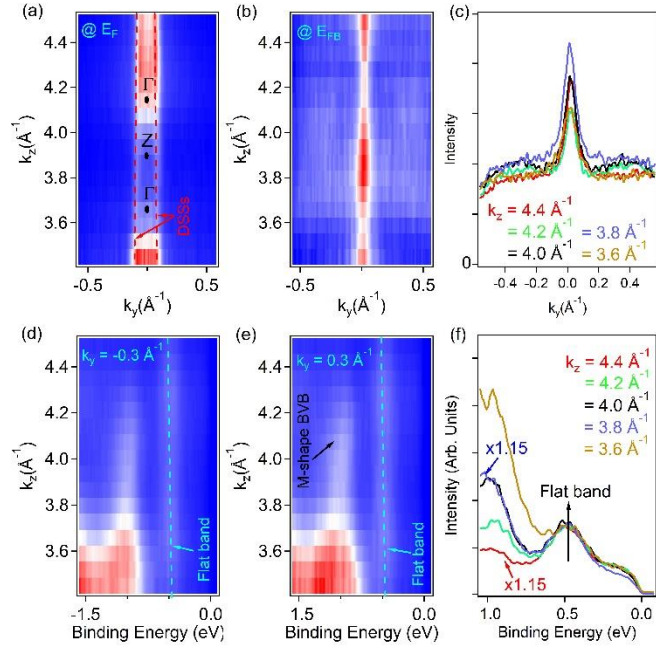


Fig. 3

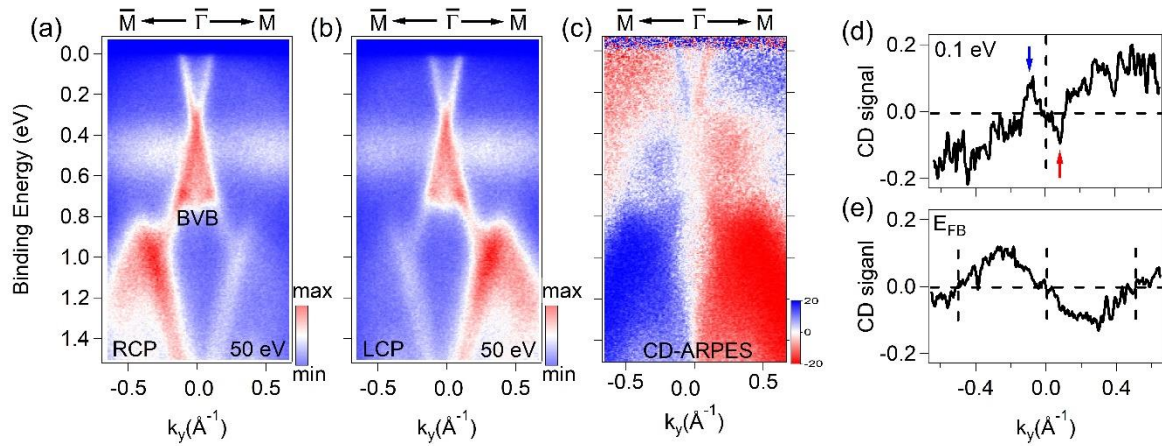


Fig. 4

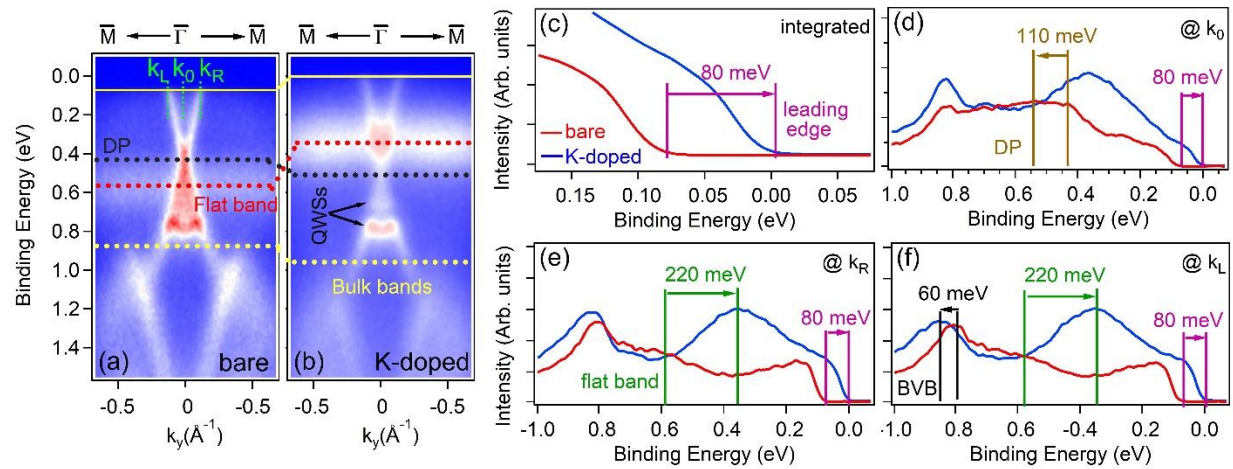


Fig. 5